Appl. Phys. B 84, 3–9 (2006)
DOI: 10.1007/s00340-006-2237-7

**Applied Physics B**
**Lasers and Optics**

E.X. JIN
X. XU✉

# Plasmonic effects in near-field optical transmission enhancement through a single bowtie-shaped aperture

School of Mechanical Engineering, Purdue University, West Lafayette, IN 47907, USA

**Received: 27 December 2005/Revised version: 31 March 2006**
**Published online: 13 May 2006 •** 

**ABSTRACT** In this paper, the enhanced optical transmission through a special type of aperture of a bowtie shape is investigated through near-field imaging and finite-difference numerical analysis. Under linear polarizations in two orthogonal directions, the optical near fields of the bowtie aperture and comparable square and rectangular apertures made in gold and chromium thin films are measured and compared. The bowtie aperture is able to provide a nanometer-sized optical spot when the incident light is polarized across the bowtie gap and delivers a considerable amount of light. Localized surface plasmons are clearly observed in the near-field images for both bowtie and rectangular apertures in gold, but invisible in chromium. Finite-difference time-domain calculations reveal that, depending on the polarization of the incident light, the unique optical properties of the bowtie aperture are a result of either the optical waveguide and the coupled surface plasmon polariton modes existing in the bowtie gap or the coupling between the two open arms of the bowtie aperture.

**PACS** 81.07.-b; 07.79.Fc; 71.36.+c; 78.66.Bz; 42.79.Gn; 42.79.Vb

## 1 Introduction

The zero-order transmission spectra through a periodic array of subwavelength holes in metal films have been shown to exhibit strong wavelength and geometry dependence and multiple transmission maxima [1], which are much larger than the value of a single hole predicted by the standard aperture theory [2]. This extraordinary optical transmission (EOT) has attracted intensive investigations in order to understand the fundamental physics involved. Further experiments have been conducted to analyze the influence of system parameters (for example, metal surface [3, 4] and hole depth [5]), as well as the reflectance and absorbance spectra [6]. Similar observations have also been made in systems working in other frequency regimes [7–9]. Despite the successful experimental demonstrations, the theoretical exploration of EOT was not straightforward. EOT was initially attributed to the surface plasmon polaritons (SPPs) [1, 6, 10–13], in which (1) the incident light is coupled to SPP modes through the momentum match provided by the periodicity of the hole array, (2) light is coupled through the holes due to the evanescent tunneling effect [14, 15], (3) SPP modes are excited on the exit side and scattered into transmitted light, again through the periodic structure, and (4) the efficient transmission occurs via the resonant excitation of SPPs on either or both sides of the metal film. In order to explain the transmission enhancement observed in hole arrays in non-metallic and perfect conductor films [16, 17], which do not inherently support SPPs, the initial SPP model was extended by including the surface EM modes [18] that can be produced by the corrugated non-metallic surfaces or perfect conductors [19].

Fundamentally, the optical transmission through a hole array is a process involving multiple diffraction of light from the periodic structure. Therefore, in principle, a complete description of the diffracted light can be obtained by solving Maxwell's equations if $\varepsilon$, $\mu$, and the geometry of the periodic structures are known. A dynamical diffraction model was proposed to describe the diffracted wave field in hole arrays in terms of Bloch wave modes [20]. It is likely that the inherently coherent diffraction of the Bloch modes (in which the SPP mode is an integral part) offers a better chance to explain the physics underlying the enhanced transmission phenomenon. However, solving the three-dimensional eigenvalue equations in terms of the complex optical properties of the metallic periodic structures is not an easy task. A simplified first-order diffraction model termed the composite diffracted evanescent wave (CDEW) model including all non-propagating components diffracted by the subwavelength feature (only one of which matches the SPP mode) was therefore proposed [16] and is able to successfully explain the transmission anomalies (both enhancement and suppression) in a simple and intuitive way. Compared to the SPP model, the CDEW model predicts both the position and the shape of the transmission peak closer to the experimental data [16] and the solution of the Maxwell equations [21]. It also explains the time delay experienced by the light passing through the hole array [22].

Orders of magnitude enhancement in transmission through hole arrays was initially claimed [1] and subsequently quoted, but a careful comparison between the transmission of a hole array and that of an isolated hole in a real metal film reveals that the transmission efficiency through the hole array can be enhanced at most by one order at the transmis-

✉ Fax: +1-765-4940539, E-mail: xxu@ecn.purdue.edu

sion peaks [16, 23]. The modest transmission enhancement through periodic arrays of subwavelength holes relative to isolated holes is mainly due to the intrinsic low transmission property of single circular apertures operated under the cutoff condition [24], i.e. the low efficiency of evanescent tunneling through non-propagating modes. In fact, there has been increased interest recently to demonstrate the effect of the aperture shape on the transmission properties [25–28]. The transmission can be further enhanced (one order higher) by using a subwavelength aperture in a rectangular shape instead of a circular one as the fundamental element of the periodic array [26]. This additional transmission enhancement is related to the excitation of localized surface plasmon (LSP) modes induced by the polarization effect [23]. The LSP modes enable the subwavelength rectangular aperture to act as a propagating waveguide [28] and increase the transmission efficiency through each aperture.

More recently, a type of unconventional aperture, a ridge aperture, has been proposed in the context of achieving both high optical transmission and subwavelength optical resolution as a single subwavelength aperture structure [29–35]. The ridge aperture, featuring a narrow gap connecting two open arms, adopts the concept of a ridge waveguide in microwave engineering [36] while having nanometric dimensions designed for optical wavelengths. As a special type of ridge aperture, a bowtie aperture has been both numerically [31, 35] and experimentally [37] demonstrated to provide a confined nanometer-scale light spot with intense optical intensity, therefore providing enhanced optical transmission at the length scale far beyond the diffraction limit. However, the mechanism of transmission enhancement through bowtie apertures has not been fully understood. In this work, we investigate the near-field optical transmission properties of bowtie apertures made in gold and chromium films. In particular, the optical near fields from the bowtie apertures and comparable regularly shaped (square and rectangular) apertures are measured using near-field scanning optical microscopy (NSOM) with a high resolution aperture probe. The effects of the polarization of incident light and the light-induced surface plasmons are investigated. Numerical computations based on the finite-difference method are performed to explore the detailed mechanism of the optical transmission enhancement through the bowtie aperture.

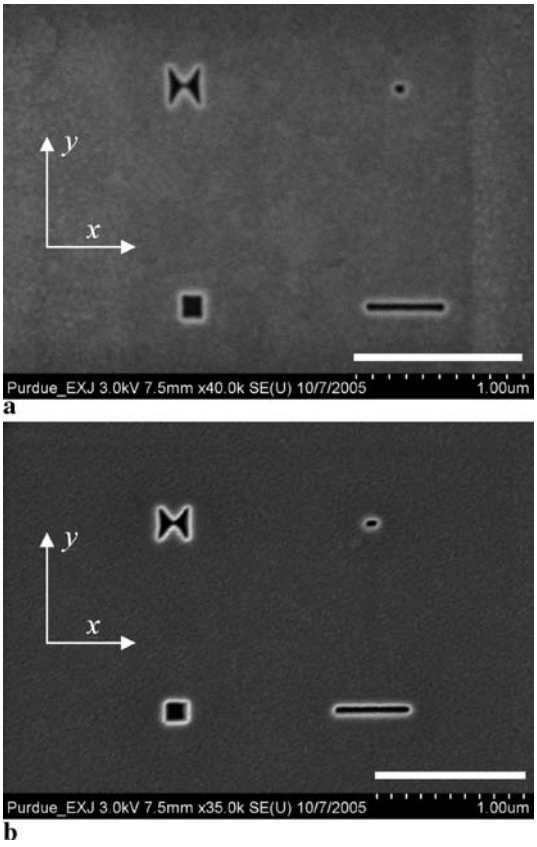


**FIGURE 1** SEM images of bowtie apertures and comparable square and rectangular apertures fabricated in (**a**) a 160-nm gold film, (**b**) a 160-nm chromium film on quartz substrates. The *scale bars* are 1 μm

## 2 Sample fabrication and the NSOM setup

Nanofabrication techniques are employed to make the bowtie apertures and comparable regular apertures in two metal films, gold and chromium. First, a gold or chromium film is deposited onto quartz substrates by e-beam evaporation. The thickness of both films is chosen to be 160 nm to limit the direct light transmission through the films. For the gold sample, a 4-nm-thick chromium film is evaporated first on the substrate as an adhesion layer. Second, the apertures are fabricated into the metal films by focused ion beam (FIB) milling (FEI Strata DB 235). The bowtie aperture is made in a 2 by 2 array together with comparable regular apertures for the purpose of comparison. The apertures are separated by more than 1 μm both in the $x$ and $y$ directions to limit the interactions among apertures. In the gold sample as shown in the scanning electron microscopy (SEM) image in Fig. 1a, the bowtie aperture has an outline of about 190 nm by 230 nm and the gap spacing between the two tips is about 36 nm, which is limited by the finite ion-beam size. A small square nanoaperture (upper right in Fig. 1a) of 36 nm by 36 nm is made to have about the same area as the gap region between the two tips of the bowtie aperture. The larger square and the rectangular apertures in the lower half of Fig. 1a are about 136 nm by 136 nm and 450 nm by 50 nm, respectively, approximately the same opening area as that of the bowtie aperture. In the chromium sample shown in Fig. 1b, the bowtie aperture has a 210 nm by 210 nm outline and a 40-nm gap, and the sizes of the other apertures are 68 nm by 50 nm, 140 nm by 140 nm, and 500 nm by 50 nm. Much larger rectangular apertures of a few microns in size are also made in both samples away from the aperture array for locating the aperture array and aligning the incident laser beam.

We use NSOM to measure the optical near field transmitted through these apertures. Our NSOM is operated in the transmission–collection mode. As schematized in Fig. 2, the aperture sample is illuminated by a linearly polarized helium–neon laser at 633-nm wavelength from the quartz-substrate side. The incident laser beam is loosely focused to a spot of tens of micrometers on the metal film. The transmitted light through the apertures is collected by a specially fabricated NSOM probe having a 65 nm by 80 nm silicon nitride core surrounded with a thin aluminum film. Detailed fabrication procedures of the NSOM probes will be presented elsewhere.

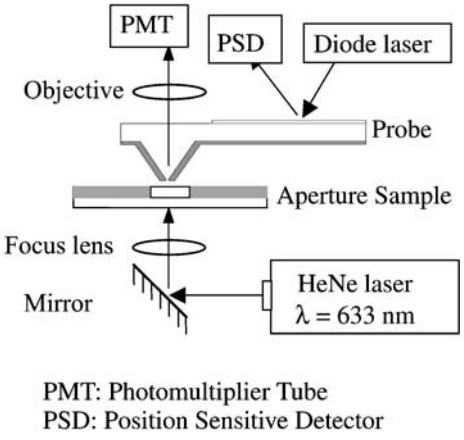


**FIGURE 2** Schematic view of near-field scanning optical microscopy (NSOM) in the illumination–collection mode to measure the optical near field from the aperture samples

A ×20 objective lens is used to direct the collected photons into a photomultiplier tube (PMT) placed in the far field. The same objective lens is also used for imaging purposes. The probe is first scanned over the sample surface in the constant-force mode. Although the resolution of the topography image (not shown here) is in the tens of nanometers range due to the finite size of the aperture probe, it can still be used to locate the aperture array. A second scan over the aperture array immediately follows and the optical signal from the PMT is recorded by a photon-counting unit to form a NSOM image. The second scan is operated in the constant-height mode in order to limit the topography effect in the NSOM image, and the distance between the probe and the surface is controlled by the normal-force feedback based on the cantilever beam deflection technique, typically in a few nanometers range. For both samples, the polarization of the illuminating laser is aligned to be either in the *y* direction across the two tips of the bowtie aperture or in the *x* direction while maintaining the same input power in order to determine the polarization dependence of light transmission through the apertures.

## 3 Experimental results and discussion

Figure 3a shows a NSOM image obtained from a 2 by 2 aperture array on the gold sample displayed in Fig. 1a, with *y*-polarized laser illumination indicated by the arrow. The NSOM image is rotated by 45° clockwise with respect to the corresponding SEM image. With constant-height scanning, the NSOM image can essentially be considered as the electric field intensity profile at a few nanometers distance away from the exit plane of the apertures [24]. It can be seen that three pronounced near-field optical spots are located in the position of three apertures but there is no discernible optical signal coming out of the smallest square aperture due to its low transmission compared to other apertures. The peak of the collected optical signal from the bowtie aperture is comparable to that from the rectangular aperture, but significantly higher than that from the square aperture. The full width at half magnitude (FWHM) of the optical spots are measured as 98 nm by 75 nm, 103 nm by 134 nm, and 186 nm by 86 nm for the bowtie, square, and rectangular apertures, respectively. Due to the convolution effect of the finite aperture probe (65 nm by 80 nm aperture size), the actual spot size should be considerably smaller than the measured ones [37]. The transmitted light spot from the bowtie aperture is much smaller than those from the comparable regular apertures and the overall size of the bowtie aperture. Considering the symmetry of the bowtie aperture and the NSOM spot, it is expected that the light is emitted from the gap of the bowtie aperture. It therefore confirms that the bowtie aperture is able to provide enhanced optical transmission at the nanometer scale.

Small signal peaks are found in the vicinity of the major optical spots of the bowtie and rectangular apertures and are distributed along the direction of polarization. These small peaks are located outside the opening area of both apertures, indicating that the detected optical emission originates from the metal surface. As will be discussed later, further near-field measurements at a different laser polarization and on the chromium sample will confirm that the origin of the small peaks is the LSPs. This direct measurement of the excitation of LSPs at near field provides experimental evidence of the role of LSPs as proposed in explaining the far-field transmission enhancement through a single rectangular aperture [38] or aperture array [23, 26, 28].

The optical transmission through apertures shows a strong polarization dependence as evidenced in the NSOM image in Fig. 3b taken with *x*-polarized illumination. First, no optical spot is found in the position of the large rectangular aperture, showing its low transmission in this polarization.

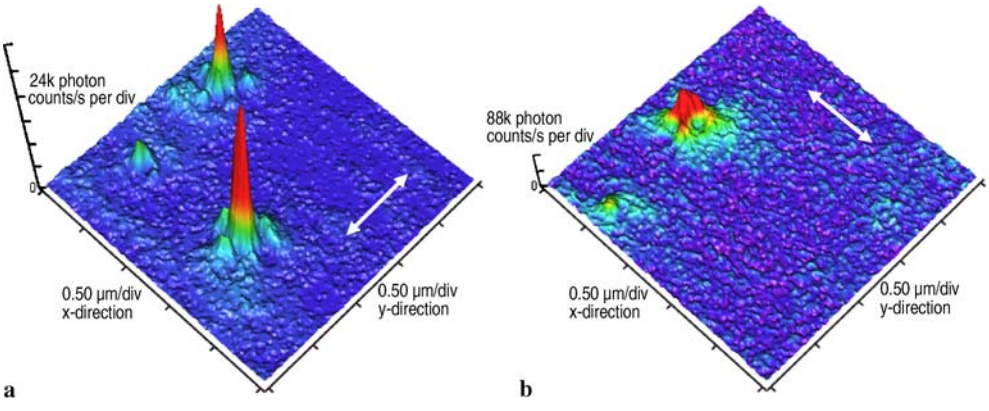


**FIGURE 3** NSOM images of aperture array in the gold sample as shown in Fig. 1a for (**a**) *y*-polarized and (**b**) *x*-polarized light. The *arrows* indicate the direction of polarization

Second, the peak signal from the larger square aperture maintains the same level as that in Fig. 3a (note that Fig. 3a and b have different scales), as expected from the symmetry of the square aperture. Third, the optical spot from the bowtie aperture is significantly enlarged and featured with two peaks. Fourth, the magnitude of the peak signal of the bowtie aperture is comparable to the other polarization. Fifth, small signal peaks are found again in the vicinity of the major peaks of the bowtie aperture but distributed along the $x$ direction, i.e. the direction of laser polarization. The polarization dependence is a key feature of LSPs, i.e. the LSPs are always excited along the direction of laser polarization, which further confirms the excitation of LSPs in shaped apertures.

We treat the square and rectangular apertures in the 160-nm-thick metal films as short optical waveguides in the $z$ direction [33]. The waveguide cutoff analysis of the optical waveguide can help us to understand the difference of near-field light transmission between the square and rectangular apertures. It is well known that the fundamental (TE mode) cutoff wavelength for a rectangular waveguide in a perfect metal is twice the side length of the rectangular cross section in the direction perpendicular to the transverse electric field. For the larger square aperture in the array, the cutoff wavelength is estimated to be about 460 nm considering the red shift of the cutoff wavelength in real metals [39], i.e. below the illumination wavelength at 633 nm for both polarizations. Since there is no propagating mode existing in the waveguide when the excitation wavelength is longer than the cutoff wavelength, an evanescent mode occurs in the square aperture and the intensity of this mode experiences exponential decay along the thickness of the metal film, resulting in the attenuated optical signal at the exit side of the aperture as seen in the NSOM images. On the other hand, the rectangular aperture has two different cutoff wavelengths depending on the polarization direction of the illuminating laser. It can support propagating modes when the helium–neon laser is $y$ polarized or significantly attenuates the $x$-polarized light as seen in Fig. 3.

The enhancement of optical transmission through bowtie apertures has been previously studied [33, 37]. It was found that, when illuminated by a $y$-polarized light beam, the bowtie aperture in aluminum is able to support a propagating waveguide mode that is localized in the bowtie gap between the two tips, which not only enhances the optical transmission but also provides a nanometer-sized near-field light spot [37]. For the bowtie aperture made in noble metals (silver or gold), in addition to the propagating waveguide mode, the SPPs excited along the walls of the bowtie gap also contribute to the transmission enhancement as will be shown later. The transmission enhancement for $x$-polarized light has not been reported in the literature. Intuitively, the two open arms of the bowtie aperture might be treated as cutoff waveguides considering their subwavelength dimensions. However, these two triangle-shaped apertures are closely connected by a narrow gap, which might introduce a coupling effect in a similar fashion as the electromagnetic coupling between adjacent nanoparticles [40] and therefore enhances the transmission for the $x$-polarized illumination. The detailed transmission mechanism of the bowtie aperture for both polarizations will be further discussed through finite-difference numerical analysis.

The apertures made in chromium shown in Fig. 1b were also investigated using NSOM. Figure 4a and b show the NSOM images for the $y$- and $x$-polarized light illuminations, respectively. For $y$-polarized illumination (Fig. 4a), the bowtie aperture results in the smallest near-field optical spot with a peak intensity slightly less than that from the rectangular aperture. The bowtie aperture has the highest optical transmission when the polarization is changed to the $x$ direction, while no light signal from the rectangular aperture can be seen in Fig. 4b. A couple of differences between the chromium and gold samples are worthy of mention. First, the peak value of the optical spot obtained from the chromium sample is weaker. Considering the identical illumination conditions, this low light transmission through the chromium film is mainly due to the smaller skin depth and larger absorption, which result from the greater absolute value of the imaginary part of the dielectric constant. The peak intensities from both the bowtie and rectangular apertures for the $y$ polarization are less in chromium than those in gold, and the square aperture in chromium did not produce transmitted light for both polarizations. Second, both the bowtie and rectangular apertures in chromium produce a clean and single optical near-field spot, lacking LSP-induced small peaks that are clearly visible in the gold sample. This confirms the previously observed LSPs in the gold sample. The excitation of LSPs is associated with strong local fields as a result of resonant oscillations of free electrons in noble metals. Noble metals, such as gold and sil-

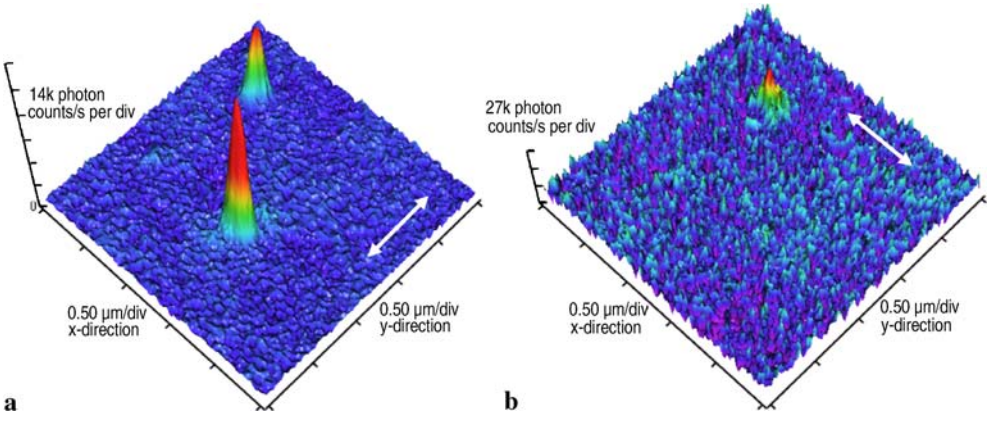


**FIGURE 4** NSOM images of aperture array in the chromium sample as shown in Fig. 1b for (**a**) $y$-polarized and (**b**) $x$-polarized light. The *arrows* indicate the direction of polarization

ver, are known to be favorable for SPP/LSP excitations since their bulk plasma frequencies are in the visible range and the imaginary part of the dielectric constant has a very small value at the SPP/LSP excitation wavelengths [41].

## 4 Finite-difference numerical analysis

To further illustrate the underlying mechanisms of the enhanced optical transmission, the finite-difference time-domain (FDTD) method [42] is used to numerically solve Maxwell's equations of light propagation through apertures. The computational system consists of a quartz substrate layer ($\varepsilon = 2.25$), a 160-nm gold or chromium film, and air on each side. The bowtie apertures with the same dimensions as the fabricated ones are configured in the middle of the films. The computational domain of 500 nm × 500 nm × 600 nm is divided into cubic Yee cells [43] of 2 nm × 2 nm × 2 nm in size to ensure that the bowtie structure is accurately represented. The six sides of the computational domain are terminated with the Liao absorbing boundary condition which provides boundary absorption in the second-order accuracy [44]. The modified Debye model [4] is employed to describe the frequency-dependent dielectric functions of gold and chromium. The parameters of the Debye model are chosen to be $\sigma = 1.592 \times 10^7$ S/m, $\varepsilon_{\text{inf}} = 10.5$, $\varepsilon_{\text{s}} = -16889.5$, and $\tau = 9.398 \times 10^{-15}$ s to closely fit the experimental data for the real and imaginary parts of the dielectric constant of gold [45] in the wavelength range between 550 and 950 nm. For chromium at 633-nm wavelength [46], the parameters of the Debye model are determined to be $\sigma = 8.62 \times 10^5$ S/m, $\varepsilon_{\text{inf}} = 1.023$, $\varepsilon_{\text{s}} = -6.92$, and $\tau = 8.16 \times 10^{17}$ s.

The incident plane wave at 633-nm wavelength illuminates the bowtie apertures from the quartz substrate side. Both polarizations of incident light used in the NSOM experiments are calculated. The FDTD results for the gold and chromium samples under $y$-polarized illumination are shown in Figs. 5 and 6, respectively. Figure 5a and b show the time-averaged $|E_y|^2$ and $|E_z|^2$ distributions in the middle $yz$ plane across the bowtie gap, and Fig. 5c and d show these two electric field components in the $xy$ plane cutting through the middle of the gold film. The $E_x$ component is orders of magnitude smaller that the other two components; therefore, it is not displayed. The $E_y$ component shows the character of a $TE_{10}$ waveguide mode from Fig. 5a and c, which is evenly distributed across the gap. The magnitude of $|E_y|^2$ is enhanced near both the entrance and exit sides of the aperture, which is associated with LSP excitation. This feature is also evident in Fig. 5b for $|E_z|^2$. It should be noted that greater enhanced fields can be introduced when LSPs are resonantly excited [35]. In Fig. 5b and d, two SPPs can be distinguished from the distribution of $|E_z|^2$ across the bowtie gap. In fact, this coupled SPP mode existing in the gap between two metallic walls has been proposed for a new type of waveguide: a metal–dielectric–metal waveguide [47, 48]. In the bowtie aperture in noble metals, the combination of the $TE_{10}$ waveguide mode and the coupled SPP mode helps to efficiently deliver the photon energy from the entrance side to the exit side of the aperture, therefore enhancing the light transmission together with the excitation of LSPs induced by the bowtie tips. In addition, both modes are localized around the nanometer-scale gap between the two bowtie tips, producing a major nanometer-sized near-field light spot as seen in the NSOM measurement (Fig. 3a). The interaction of LSPs with the NSOM probe results in side peaks with less intensity in the NSOM image. The obtained NSOM image of the bowtie aperture can therefore be regarded as the coupling of the near-field probe with the field intensity distri-

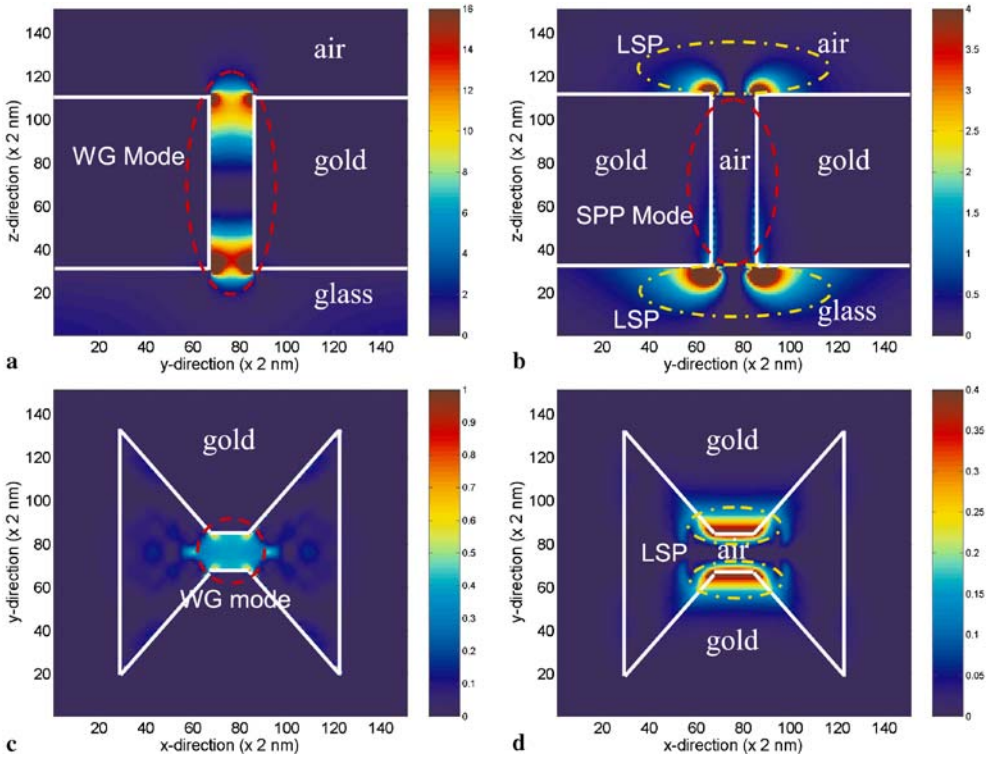


**FIGURE 5** Time-averaged (**a**), (**c**) $|E_y|^2$ and (**b**), (**d**) $|E_z|^2$ distributions of the bowtie aperture in a 160-nm gold film on quartz substrate computed by the FDTD method. The $y$-polarized plane wave at 633-nm wavelength is incident from the substrate side. (**a**), (**b**) show the middle $yz$ plane across the bowtie gap, and (**c**), (**d**) show the $xy$ plane cutting through the middle of the gold film

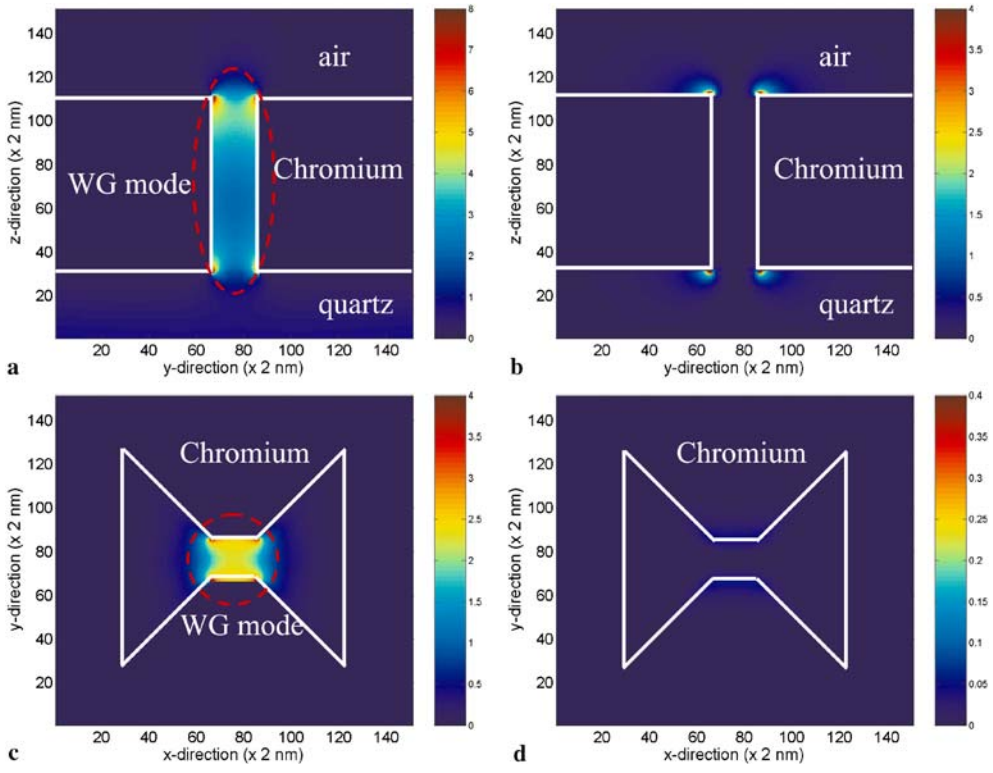


**FIGURE 6** Time-averaged (**a**), (**c**) $|E_y|^2$ and (**b**), (**d**) $|E_z|^2$ distributions of the bowtie aperture in a 160-nm chromium film on quartz substrate computed by the FDTD method. The *y*-polarized plane wave at 633-nm wavelength is incident from the substrate side. (**a**), (**b**) show the middle *yz* plane across the bowtie gap, and (**c**), (**d**) show the *xy* plane cutting through the middle of the chromium film

butions on the exit plane of the aperture, which are similar to what are shown in Fig. 5c and d. For the bowtie aperture in the chromium film, the FDTD numerical results show that there is no SPP mode in the aperture (Fig. 6b and d). The $TE_{10}$ waveguide mode is dominant in the process of light propagation as shown in Fig. 6a and c. The *z* component of the electric field at the edges in both the entrance and exit planes of the bowtie aperture (see Fig. 6b) is caused by the scattering effect [35], but its intensity is less than the LSP-induced field as compared with the bowtie aperture in the gold film. As a result, a single and clean optical spot is found in the NSOM image as shown in Fig. 4a.

Figure 7 shows the computational results for the bowtie aperture in the gold film under *x*-polarized illumination. Complicated distributions of the electric field are found inside the aperture, which are no longer confined in the gap area but located in the two open arms, therefore resulting in a near-field spot comparable to the overall area of the bowtie aperture. Similar results are seen for the bowtie aperture in the chromium film, which is not displayed here. Therefore, the FDTD calculations agree with the NSOM measurements in that the transmitted spots at *x* polarization are larger than those at *y* polarization. It is possible that the coupling of the two open arms increases the cutoff property of a single triangular aperture, allowing complicated propagating waveguide modes in the bowtie aperture.

## 5 Conclusions

Enhanced optical near-field transmission from bowtie apertures fabricated in gold and chromium films was observed via NSOM measurements operated in the illumination–collection mode. Compared to square and rectangular apertures of the same opening area, the bowtie aperture is able to provide a nanometer-sized near-field optical spot for the incident light polarized across the bowtie gap.

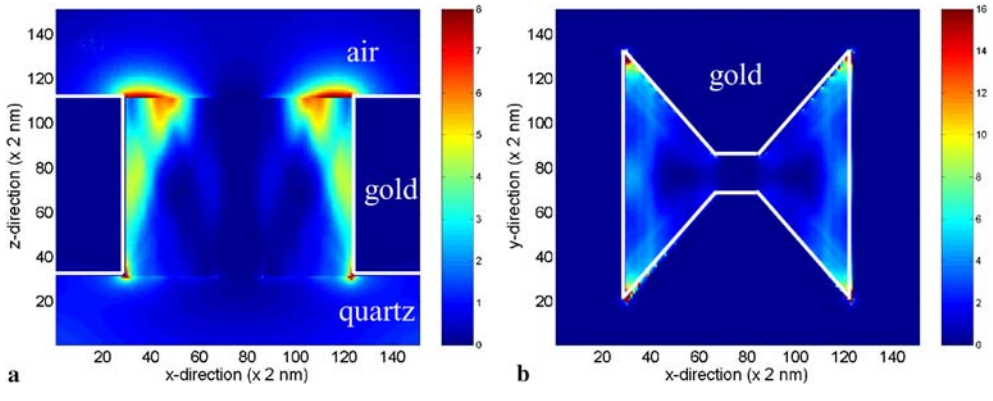


**FIGURE 7** Time-averaged $|E|^2$ distributions of the bowtie aperture in a 160-nm gold film on quartz substrate computed by the FDTD method. The *x*-polarized plane wave at 633-nm wavelength is incident from the substrate side. (**a**) shows the middle *xz* plane cutting through the middle of the bowtie gap, and (**b**) shows the *xy* plane cutting through the middle of the gold film

The bowtie aperture also delivers a considerable amount of light when the polarization of the incident light is rotated by 90°. The transmission through the rectangular aperture, on the other hand, strongly depends on the polarization due to the high aspect ratio of the two side lengths. LSPs are observed in the NSOM images for both bowtie and rectangular apertures in gold, but invisible in chromium. The LSP excitation further enhances the transmission through the apertures but introduces side peaks around the major optical spot. FDTD computations reveal that the coupled SPP mode assists the $TE_{10}$ waveguide mode to efficiently deliver the photon energy from the entrance to the exit of the bowtie aperture in the gold film when the incident light is polarized across the bowtie gap, and the coupling of the two open arms enables the bowtie aperture to act as a propagating waveguide when the polarization of the incident light is changed to the orthogonal direction.

**ACKNOWLEDGEMENTS** The financial support of this work by the National Science Foundation is gratefully acknowledged. Fabrication of the aperture samples by FIB machining was carried out in the Center for Microanalysis of Materials, University of Illinois, which is partially supported by the US Department of Energy under Grant No. DEFG02-91-ER45439.

## REFERENCES

1 T.W. Ebbesen, H.J. Lezec, H.F. Ghaemi, T. Thio, P.A. Wolff, Nature **391**, 667 (1998)
2 H. Bethe, Phys. Rev. **66**, 163 (1944)
3 D.E. Grupp, H.J. Lezec, T.W. Ebbesen, K.M. Pellerin, T. Thio, Appl. Phys. Lett. **77**, 1569 (2000)
4 T. Thio, H.F. Ghaemi, H.J. Lezec, P.A. Wolff, T.W. Ebbesen, J. Opt. Soc. Am. B **16**, 1743 (1999)
5 A. Degiron, H.J. Lezec, W.L. Barnes, T.W. Ebbesen, Appl. Phys. Lett. **81**, 4327 (2002)
6 W.L. Barnes, W.A. Murray, J. Dintinger, E. Devaux, T.W. Ebbesen, Phys. Rev. Lett. **92**, 107 401 (2004)
7 S. Williams, A. Stafford, T. Rogers, S. Bishop, J. Coe, Appl. Phys. Lett. **85**, 1472 (2004)
8 J. Rivas, C. Schotsch, P. Bolivar, H. Kurz, Phys. Rev. B **68**, 201 306 (2003)
9 H. Cao, A. Nahata, Opt. Express **12**, 1004 (2004)
10 H. Ghaemi, T. Thio, D. Grupp, T.W. Ebbesen, H. Lezec, Phys. Rev. B **58**, 6779 (1998)
11 E. Popov, M. Neviere, S. Enoch, R. Reinisch, Phys. Rev. B **62**, 16 100 (2000)
12 L. Martín-Moreno, F. García-Vidal, H. Lezec, K. Pellerin, T. Thio, J. Pendry, T.W. Ebbesen, Phys. Rev. Lett. **86**, 1114 (2001)
13 A. Krishnan, T. Thio, T. Kima, H. Lezec, T. Ebbesen, P. Wolff, J. Pendry, L. Martín-Moreno, F. García-Vidal, Opt. Commun. **200**, 1 (2001)
14 W. Liu, D. Tsai, Phys. Rev. B **65**, 155 423 (2002)
15 S. Darmanyan, A. Zayats, Phys. Rev. B **67**, 035 424 (2003)
16 H. Lezec, T. Thio, Opt. Express **12**, 3629 (2004)
17 H. Sarrazin, J.-P. Vigneron, Phys. Rev. E **68**, 016 603 (2003)
18 L. Martín-Moreno, F. García-Vidal, Opt. Express **12**, 3619 (2004)
19 J.B. Pendry, L. Martín-Moreno, F. García-Vidal, Sci. Express **10**, 1126 (2004)
20 M. Treacy, Phys. Rev. B **66**, 195 105 (2002)
21 F. García-Vidal, H. Lezec, T. Ebbesen, L. Martín-Moreno, Phys. Rev. Lett. **90**, 213 901 (2003)
22 A. Dogariu, T. Thio, L. Wang, T. Ebbesen, H. Lezec, Opt. Lett. **26**, 450 (2001)
23 A. Degiron, T. Ebbesen, J. Opt. A **7**, S90 (2005)
24 S.-H. Chang, S.K. Gray, G.C. Schatz, Opt. Express **13**, 3150 (2005)
25 R. Gordon, A. Brolo, A. McKinnon, A. Rajora, B. Leathem, K. Kavanagh, Phys. Rev. Lett. **92**, 037 401 (2004)
26 K.J.K. Koerkamp, S. Enoch, F.B. Segerink, N.F. van Hulst, L. Kuipers, Phys. Rev. Lett. **92**, 183 901 (2004)
27 H. Cao, A. Nahata, Opt. Express **12**, 3664 (2004)
28 K.L. van der Molen, K.J.K. Koerkamp, S. Enoch, F.B. Segerink, N.F. van Hulst, L. Kuipers, Phys. Rev. B **72**, 045 421 (2005)
29 X. Shi, L. Hesselink, Jpn. J. Appl. Phys. **41**, 1632 (2002)
30 K. Tanaka, M. Tanaka, J. Microsc. **210**, 294 (2002)
31 K. Sendur, W. Challener, J. Microsc. **210**, 279 (2002)
32 A.V. Itagi, D.D. Stancil, J.A. Bain, T.E. Schlesinger, Appl. Phys. Lett. **83**, 4474 (2003)
33 E.X. Jin, X. Xu, Jpn. J. Appl. Phys. 1 **43**, 407 (2004)
34 J. Matteo, D. Fromm, Y. Yuen, P. Schuck, W. Moerner, L. Hesselink, Appl. Phys. Lett. **85**, 648 (2004)
35 E.X. Jin, X. Xu, Appl. Phys. Lett. **86**, 111 106 (2005)
36 J. Helszajn, *Ridge Waveguides and Passive Microwave Components* (IEE, London, 2000)
37 E.X. Jin, X. Xu, Appl. Phys. Lett. **88**, 153 110 (2006)
38 A. Degiron, H.J. Lezec, N. Yamamoto, T.W. Ebbesen, Opt. Commun. **239**, 61 (2004)
39 R. Gordon, A.G. Brolo, Opt. Express **13**, 1933 (2005)
40 S.A. Maier, P.G. Kik, H.A. Atwater, Appl. Phys. Lett. **81**, 1714 (2002)
41 H. Raether, *Surface Plasmons on Smooth and Rough Surfaces and on Gratings* (Springer, Berlin, 1988)
42 K. Kunz, R. Luebbers, *The Finite Difference Time Domain Method for Electromagnetics* (CRC, Boca Raton, FL, 1996)
43 S. Yee, IEEE Trans. Antennas Propag. **14**, 302 (1966)
44 Z.P. Liao, H.L. Wong, G.P. Yang, Y.F. Yuan, Sci. Sin. **28**, 1063 (1984)
45 P.B. Johnson, R.W. Christy, Phys. Rev. B **6**, 4370 (1972)
46 D.R. Lide, *CRC Handbook of Chemistry and Physics* (CRC, Boca Raton, FL, 1996)
47 K. Tanaka, M. Tanaka, Appl. Phys. Lett. **82**, 1158 (2003)
48 B. Wang, G.P. Wang, Appl. Phys. Lett. **85**, 3599 (2004)